8-2016

Enhanced and tunable optical quantum efficiencies from plasmon bandwidth engineering in bimetallic CoAg nanoparticles

A. Malasi
University of Tennessee, Knoxville

H. Taz
University of Tennessee, Knoxville

M. Ehrsam
University of Tennessee, Knoxville

J. Goodwin
Webb School of Knoxville

H. Garcia
Southern Illinois University Edwardsville

See next page for additional authors

Recommended Citation

Malasi, A., Taz, H., Ehrsam, M., Goodwin, J., Garcia, H., & Kalyanaraman, R. (2016). Enhanced and tunable optical quantum efficiencies from plasmon bandwidth engineering in bimetallic CoAg nanoparticles. APL Photonics, 1(7), 076101. doi: 10.1063/1.4954698

AIP | APL Photonics

Enhanced and tunable optical quantum efficiencies from plasmon bandwidth engineering in bimetallic CoAg nanoparticles

A. Malasi, H. Taz, M. Ehrsam, J. Goodwin, H. Garcia, and R. Kalyanaraman

Citation: APL Photonics **1**, 076101 (2016); doi: 10.1063/1.4954698
View online: http://dx.doi.org/10.1063/1.4954698
View Table of Contents: http://scitation.aip.org/content/aip/journal/app/1/7?ver=pdfcov
Published by the AIP Publishing

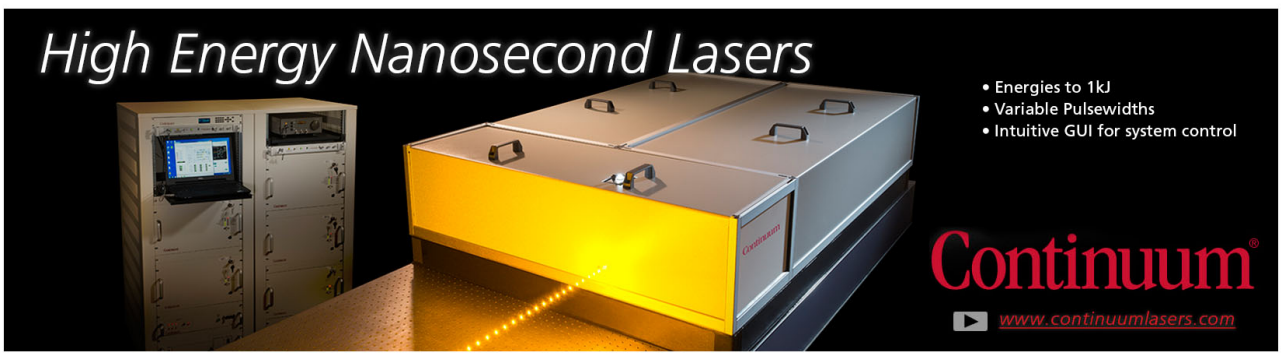

APL PHOTONICS **1**, 076101 (2016)

Enhanced and tunable optical quantum efficiencies from plasmon bandwidth engineering in bimetallic CoAg nanoparticles

A. Malasi,[1] H. Taz,[2] M. Ehrsam,[3] J. Goodwin,[4] H. Garcia,[5] and R. Kalyanaraman[1,2,6,a]

[1]*Department of Chemical and Biomolecular Engineering, University of Tennessee, Knoxville, Tennessee 37996, USA*
[2]*Bredesen Center, University of Tennessee, Knoxville, Tennessee 37996, USA*
[3]*Department of Mechanical, Aerospace and Biomedical Engineering, University of Tennessee, Knoxville, Tennessee 37996, USA*
[4]*Webb School of Knoxville, Knoxville, Tennessee 37923, USA*
[5]*Department of Physics, Southern Illinois University, Edwardsville, Illinois 62026, USA*
[6]*Department of Material Science and Engineering, University of Tennessee, Knoxville, Tennessee 37996, USA*

(Received 28 March 2016; accepted 12 June 2016; published online 1 August 2016)

Plasmonic nanoparticles are amongst the most effective ways to resonantly couple optical energy into and out of nanometer sized volumes. However, controlling and/or tuning the transfer of this incident energy to the surrounding near and far field is one of the most interesting challenges in this area. Due to the dielectric properties of metallic silver (Ag), its nanoparticles have amongst the highest radiative quantum efficiencies (η), i.e., the ability to radiatively transfer the incident energy to the surrounding. Here we report the discovery that bimetallic nanoparticles of Ag made with immiscible and plasmonically weak Co metal can show comparable and/or even higher η values. The enhancement is a result of the narrowing of the plasmon bandwidth from these bimetal systems. The phenomenological explanation of this effect based on the dipolar approximation points to the reduction in radiative losses within the Ag nanoparticles when in contact with cobalt. This is also supported by a model of coupling between poor and good conductors based on the surface to volume ratio. This study presents a new type of bandwidth engineering, one based on using bimetal nanostructures, to tune and/or enhance the quality factor and quantum efficiency for near and far-field plasmonic applications. [http://dx.doi.org/10.1063/1.4954698]

I. INTRODUCTION

One of the most interesting properties demonstrated by metal nanoparticles is their strong resonant response to electromagnetic (EM) fields. In general, when photons strike a metal nanoparticle, whose size is comparable to or smaller than the wavelength of light, it can induce collective coherent oscillations of the electrons of the metal. For nanoparticles, these oscillations occur at specific frequency known as the plasmon frequency or the localized surface plasmon resonance (LSPR) frequency.[1] The primary outcome of this interaction can be broadly categorized as being twofold. On one hand, a very efficient scattering of photons takes place, thus making plasmonic nanoparticles very important for applications pertaining to photon redirection and/or transfer, such as in wave guiding, for light trapping inside thin film solar cells, and in optical computing requiring the efficient bending of light in small volumes.[2–6] On the other hand, plasmonic resonances are also associated with enhanced

[a]Electronic address: ramki@utk.edu

photon absorption within the nanoparticle. The subsequent conversion of this absorbed energy for the generation of charge carriers and/or phonons has been considered in applications such as photocatalysis, photothermal imaging, plasmonic heating, and heat-assisted magnetic recording.[4,7–9] In this context, one of the exciting challenges in the field of plasmonic nanostructures is understanding how to tune and/or control the plasmonic interaction process such that the material can be optimized to show either enhanced radiative effects or enhanced absorptive (non-radiative) effects.

The properties of the resonant plasmon interaction, such as the location of the plasmon frequency and the intensity of the resonance, such as determined by the plasmon bandwidth, depend intrinsically on the metal-type, and extrinsically on such factors as the shape, size, and nature of the surrounding medium.[4,10–12] Therefore, it is natural to expect that optimizing the radiative versus non-radiative effects will also depend on these parameters. Indeed, as was first demonstrated by Sonnichsen *et al.*, it is possible to tune the plasmonic bandwidth by changing the shape of the nanoparticle such that the dominant process changes from non-radiative loss inside the nanoparticle to radiative damping.[10] However, controlling the shape is not always straightforward and so other means are being sought to tune plasmonic properties. Recently, there has been substantial interest in using multimetallic nanoparticles, either in the form of alloys or other segregated structures, such as core-shell, layered discs, and Janus faced particles, to better tune these plasmonic properties.[13–19] It has been seen that on combining two different metals new phenomenon and/or improved properties can be observed. For example, in core-shell nanoparticles of Au-Ag, the plasmon resonance energy of the Au core could be decreased from 500 to 400 nm by increasing the Ag shell thickness.[13] By synthesizing bimetals that combine metals with large intrinsic magneto-optical (MO) activity, such as ferromagnets, with metals with large intrinsic plasmonic resonances, such as the noble metals, the MO activity of the bimetal can be significantly enhanced. For instance, core-shell nanoparticles of Co-Ag show much higher Faraday rotation than pure Co when measured at the plasmon resonance frequency of the bimetal nanoparticle.[14] Plasmonic nanosandwiches consisting of Au/Co/Au system have also demonstrated enhanced MO activity at the LSPR of the nanosandwich.[15] The MO activity and the LSPR of the nanosandwich can be further tuned by controlling the thickness of the individual metal layers or the diameter of the nanosandwich.[15,20] However, to our knowledge, alloying and/or physical contact of two different metals has not been shown to lead to localized surface plasmon resonances that are sharper than those present in the better plasmonic metal making up the constituent. In other words, multimetallic nanostructures are generally more suitable for applications in which the non-radiative energy loss channel is preferable.

Here we present an experimental study comparing the plasmonic properties of ensembles of Ag nanoparticles to those of CoAg bimetallic nanoparticles. These studies demonstrated that the bimetal CoAg nanoparticles can show a lowering of the bandwidth over that of the most superior plasmonic metal, Ag under certain volume and energy conditions. As a result, the bimetal showed comparable or better quality factor and quantum efficiencies, i.e., the radiative scattering process, with respect to pure Ag.

II. RESULTS

A. Optical spectroscopy of Ag nanoparticles

We begin with detailing the plasmonic properties of Ag nanoparticle (NP) arrays prepared by pulsed laser dewetting on transparent glass substrates. Fig. 1(a) is a representative scanning electron microscopy (SEM) image of freshly prepared array of Ag NPs synthesized by pulsed laser dewetting of ~1.5 nm thick Ag film. The inset of the image shows the size histogram of the particle size, which conveyed a monomodal distribution with an average particle diameter of 36 ± 11 nm. Such particles have been well documented to have a nearly hemispherical shape,[21–26] and therefore, the average particle diameter could be translated into an average particle volume for the array. By performing laser dewetting with Ag films of varying initial film thickness, we created a number of arrays containing particles whose average diameter (D) varied from ~25 to 120 nm, corresponding to an average particle volume ($\pi D^3/12$) ranging between ~4×10^3 and 5×10^5 nm^3.

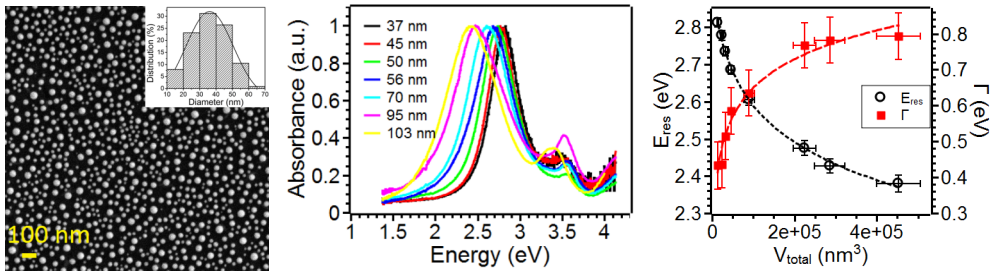

FIG. 1. (a) SEM image of pure Ag NP array of size 36 ± 11 nm with the particle size distribution histogram is in the inset. (b) The normalized absorption spectrum of different sized hemispherical NPs plotted as a function of energy. (c) The plasmon resonance energy and the bandwidth are plotted as a function of Ag NP size. The black hollow circles and the solid red squares denote plasmon resonance energy and the bandwidth, respectively. The black dotted and the dashed red lines are the best fits for the experimental data.

Fig. 1(b) shows the normalized broadband absorption spectrum vs photon energy for the Ag NP arrays as a function of average diameter. The maxima in the absorption spectra corresponds to the position of the localized surface plasmon resonance (LSPR) or plasmon resonance energy (E_{res}) for the nanoparticle array. It can be seen from Fig. 1(b) that as the average NP diameter increased the plasmon resonance energy decreased (i.e., plasmon red shifted). Another feature that was evident was the broadening in the absorption spectrum, i.e., the bandwidth of the peak increased. Both these features are consistent with the size-dependent behavior of nanoparticles.[1] From the optical spectra in Fig. 1(b), it was possible to generate the trend in plasmon resonance energy and the energy bandwidth (Γ) as a function of particle volume, and this is shown in Fig. 1(c). In Fig. 1(c) the left y-axis corresponds to the plasmon resonance energy shown by the black hollow circles and the right y-axis is for the energy bandwidth shown by solid red squares. Guides to the eye are shown by the black dotted and red dashed lines, respectively. The energy bandwidth was obtained from the absorption spectra by fitting a single Lorentzian peak at the resonance energy as shown in the supplementary material. It is worth mentioning that since this bandwidth is from a nanoparticle array with a finite size distribution, it will also intrinsically include contributions from in-homogeneous broadening that arise due to the different size-dependent contributions to broadening. In-homogeneous broadening can be quantified by a Gaussian correction to the Lorentzian line shape of the plasmonic signal. However, as we show in the supplementary material, when the spectra were fitted to a single Lorentz shape, an excellent fit, with regression values of $R^2 > 0.90$ was consistently obtained and we concluded that the Gaussian contribution was much less than the uncertainty of fitting. Therefore, the bandwidth values presented throughout this manuscript were based on a single Lorentz peak fit of the absorbance spectra. From Fig. 1(c) it was clear that the energy bandwidth increased with increasing volume (diameter) of the Ag NPs.

B. Bimetallic CoAg nanostructures

Next, we performed a similar optical study of bimetallic CoAg nanoparticles with varying diameter and composition by dewetting of bilayer films by a process described previously.[22,27] In brief, laser melting of bilayer films consisting of a bottom Ag film with thickness fixed at 5 nm and a top Co film with thickness varied from 1 to 5 nm was performed on glass substrates. From this, different compositions and volumes of CoAg bimetal NPs were obtained. A representative SEM of a CoAg NP array synthesized by laser dewetting of a bilayer consisting of 2 nm thick Co on 5 nm thick Ag layer is shown in Fig. 2(a). Shown in the inset is the size histogram again conveying the monomodal size distribution of particles with average size of 113 ± 30 nm. The shapes of these Ag-Co nanoparticles have also been previously confirmed to be near hemispherical.[22–24] In addition, these works have confirmed that in this metallurgically immiscible system, the Ag and Co occupy distinct segregated regions within the nanoparticle. The normalized absorption spectra of various CoAg arrays are shown

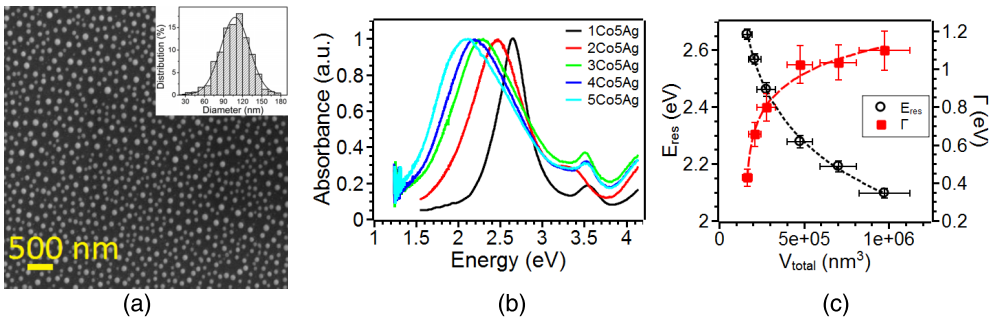

FIG. 2. (a) Representative SEM image of Co-Ag NP system. The SEM corresponds to Co (2 nm)/Ag (5 nm) with the average NP size of 113 ± 30 nm. The inset shows the size distribution histogram. (b) Corresponds to the normalized absorption spectrums of Co-Ag bimetallic system. The Ag film thickness is fixed at 5 nm and the Co thickness is varied from 1-5 nm. (c) Plots the plasmon energy as a function of NP size for the Co-Ag systems.

in Fig. 2(b). Fig. 2(c) compares the plasmon resonance energy and the bandwidth of the bimetallic systems as a function of the total volume of the NP, again estimated from the average particle diameter. It was seen that on increasing the NP volume, the plasmon red shifted, consistent with previous reports on such bimetallic systems.[22,28] The bandwidth also increased on increasing the NP volume. These general trends appeared similar to those found for pure Ag nanoparticles presented in Fig. 1(c), i.e., the bandwidth increased with increasing particle volume. However, some very unexpected attributes were observed for the bimetal nanoparticles upon comparing to pure Ag, as we discuss in Subsection II C.

C. Quality factor of hemispherical Ag versus CoAg

The quality factor of a plasmon resonance is one of the most important characteristics in determining the usefulness of a material for plasmonic sensing applications. The quality factor can be calculated experimentally through the function $Q = \frac{E_{res}}{\Gamma}$, where E_{res} corresponds to the resonance energy and Γ is the energy bandwidth. As detailed in Ref. 29, the quality factor is a measure of how effectively the nanoparticle interacts with light, and only a few metals (Ag, Au, etc.) show strong interactions (resonances) because of their high Q. One of the direct impacts of the quality factor is the ability of nanoparticles to sense changes in their local environment, which is the basis for the technique of localized surface plasmon resonance sensing or LSPR sensing. It is well known that particle with higher quality factor show higher sensitivity to detection.[30] A second characteristic highly relevant to many plasmonic applications is the ability of the plasmonic nanoparticle to efficiently couple with light and subsequently transfer photons into the surrounding environment, as would be needed in imaging or solar energy harvesting. This ability is measured by the quantum efficiency η, which is defined as $\eta = \frac{\Gamma_{1R}}{\Gamma_{1R}+\Gamma_{1NR}}$, where the various quantities are the radiative energy bandwidth (Γ_{1R}) and the non-radiative energy bandwidth (Γ_{1NR}). Despite a large number of investigations of the plasmonic quality factor of nanoparticles as a function of material, shape, and size, there is very little known about the quality and quantum efficiency of hemispherical shaped particles of Ag or bimetallic Ag.

Here we compared these characteristics of the two systems, as shown in Fig. 3, where the experimentally calculated quality factor using the results from Figs. 1(c) and 2(c) are shown for the Ag and CoAg nanoparticles, respectively. In Fig. 3(a), the Q is shown as a function of the effective Ag volume within the nanoparticle. For the case of Ag, this corresponds directly to the Ag NP volume, while, for the case of CoAg, this Ag volume was estimated based on the thickness ratio of the bimetal films from which it was created. As has been shown previously by elemental characterization studies, the average metallic content within the CoAg bimetal particles is identical to the ratio of the starting bilayer film thickness.[22] From the trend in the experimental data shown in Fig. 3(a), it was evident that the Q values of the bimetal could become comparable to or better than Ag for average volumes $\lesssim 2 \times 10^5$ nm^3 (corresponding to a hemispherical particle of diameter $\lesssim$90 nm). This is an especially interesting result given that mixing of metals generally leads to a degradation in the plasmonic property when measured with respect to the pure plasmonic metal.[29] In Fig. 3(b) the Q is shown as a function of

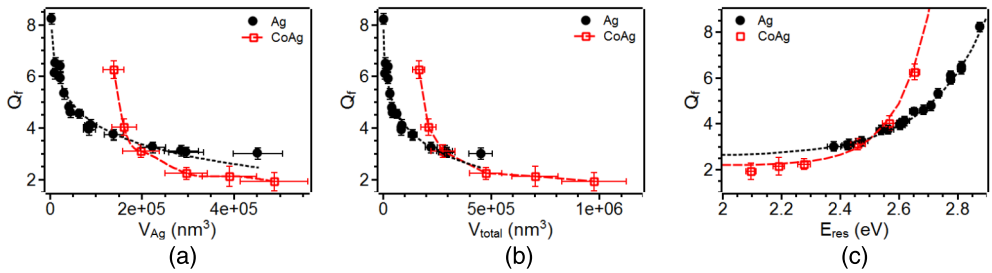

FIG. 3. Quality factor for Ag versus CoAg in air. (a) Dependence of Q on the effective volume of Ag within the nanoparticle. (b) Dependence of Q on the total volume of nanoparticle. (c) Dependence of Q on resonance (LSPR) energy.

the total volume of the particle, i.e., volume of pure Ag and the CoAg. Once again, from the trends in the experimental data (symbols), it was clearly evident that for total volumes $\lesssim 2.5 \times 10^5$ nm^3, the CoAg has comparable or better Q than an equivalent volume of Ag. This interesting behavior was also clearly evident when the Q was plotted as a function of the resonance energy, Fig. 3(c), where, for $E_{res} \gtrsim 2.5$ eV, the bimetal had comparable or better quality plasmons than pure Ag.

III. DISCUSSION

We first attempted to interpret the results by the use of an effective medium approach (EMA) in which the bimetallic nanoparticle can be treated as being made from a metal with an effective dielectric function that is related to the volume fraction of the two metals, in this case Ag and Co. The effective dielectric of the bimetal NP, $\epsilon_{eff,NP}$, was calculated using the mixing model suggested in References 26, 28, and 31

$$\epsilon_{eff,NP} = \left(\frac{f}{\epsilon_1} + \frac{(1-f)}{\epsilon_2} - \frac{2f(1-f)(\epsilon_1-\epsilon_2)^2}{3\epsilon_1\epsilon_2(\epsilon_2\gamma + \epsilon_1(1-\gamma))} \right)^{-1}, \tag{1}$$

where ϵ_1 and ϵ_2 correspond to the complex dielectric of the constituent metals, f is the volume fraction of the metals in a single nanoparticle, and γ is a NP shape parameter. Following this, the effective dielectric of the nanoparticles on a substrate was calculated using an EMA specifically developed to capture the size-dependent plasmonic behavior of particles in the Mie limit, i.e., where particles with large size can also be evaluated.[32] The optical density of the CoAg NPs was calculated by considering them embedded in a dielectric slab of $n = 1.3$. The total complex effective dielectric of the dielectric slab with embedded nanoparticles was calculated as described in Ref. 32. The effective complex dielectric of the slab was calculated using the following relation:

$$\epsilon_{total} = \epsilon_h - \frac{\frac{3f'\epsilon_h}{2q^3}\mathrm{Im}\left\{\sum_{l=1} i(2l+1)({}^e a_l + {}^m b_l)\right\}}{1 + \frac{f'}{2q^3}\mathrm{Im}\left\{\sum_{l=1} i(2l+1)({}^e a_l + {}^m b_l)\right\}}, \tag{2}$$

where ϵ_h is the dielectric of the host medium, and f' is the volume fraction of NPs in the slab. a and b correspond to the Mie coefficients given in terms of Ricaty-Bessel cylindrical functions, e and m are the electric and magnetic multipoles, l corresponds to the pole contributions, and $q = \frac{\pi Dn}{\lambda}$ is a size parameter.

In Fig. 4 we show the quality factor predicted from this Mie model for spherically shaped bimetals of CoAg. In Fig. 4(a) the total particle volume was fixed, whereas in the inset figure, the volume of Ag was fixed while the volume of Co was varied. It was evident that in all cases, the addition of Co decreased the Q-factor over that of pure Ag. This behavior can be understood from the nature of the imaginary components of the dielectric functions of Ag and Co, which is shown in Fig. 4(b). It is evident that in the energy range investigated in this work, the imaginary component of Co is significantly larger than that of Ag and therefore an effective medium approach will predict a lower Q factor than the pure Ag metal. In fact, for any combination of metals, the Q factor calculated using EMA will

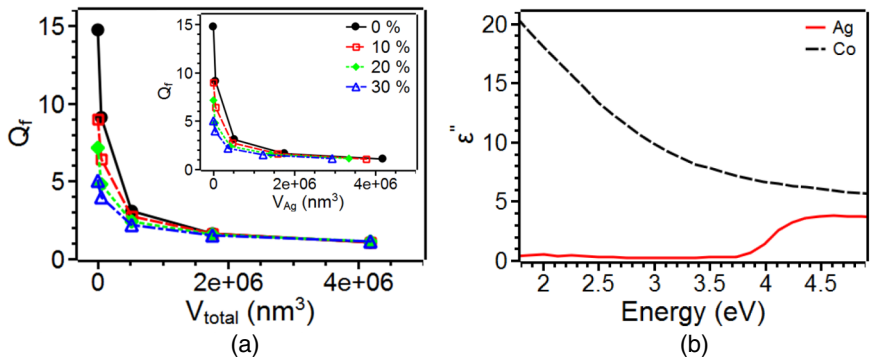

FIG. 4. (a) The quality factor for CoAg bimetal spheres calculated using Mie theory with an effective medium approach to calculate the dielectric function. The quality factor of the CoAg bimetal is plotted as a function of total nanoparticle volume and in the inset the quality factor is plotted as a function of Ag volume in the nanoparticle. (b) Imaginary component of the dielectric function ε'' of Ag (solid line) and Co (dashed line) as a function of energy.

always be lower than the value of the better plasmonic metal. This result hinted to a fundamentally different behavior being shown in this nanostructured system.

Next, we interpreted the change in bandwidth for plasmonic absorption based on the two-level model, analogous to molecular spectroscopy, in which the plasmon decays by dephasing of the coherent oscillations at a total rate given by[33]

$$\Gamma_2 = \frac{\hbar}{T_2} = \frac{\hbar}{2T_1} + \frac{\hbar}{T_2^*}, \tag{3}$$

where c is the speed of light, $\hbar$ is Planck's constant, T_1 is the electron relaxation time due to inelastic processes such as radiative loss and non-radiative absorption, and T_2^* is the dephasing due to elastic scattering processes such as electron collision with other electrons, defects, and/or surfaces. Since the inelastic process has contributions primarily from radiative loss, i.e., emission of photons, and non-radiative damping, such as due to intra- and inter-band transitions of electrons,[34] so the total dephasing energy bandwidth can be expressed as

$$\Gamma_2 = \frac{1}{2}\Gamma_{1,R} + \frac{1}{2}\Gamma_{1,NR} + \Gamma *_2, \tag{4}$$

where the subscripts R and NR refer to radiative and non-radiative components, respectively. To interpret our experimental data we simplified this function based on certain approximations valid in the particle size range of our investigations (i.e., 20–200 nm) as discussed next.

1. *Dephasing by electron scattering*: The broadening of the plasmon peak due to elastic scattering is a result of many events happening locally such as electron-electron, electron-phonon, electron-defect, and electron-surface scattering processes.[35,36] The damping constant (inverse of the electron relaxation times) of these events follows Mathiessen's rule where the scattering rates can be added because they are statistically independent channels. In bulk materials, electron-phonon scattering dominates, but as the size of the NP is decreased other events start to dominate. For a NP whose size is comparable to the mean free path of electrons, electron-surface scattering is a dominant effect and in the simplest model the size-dependent elastic dephasing energy rate is given by

$$\frac{\hbar}{T_2^*} = \frac{\hbar}{T_2^o} + A\frac{2\hbar v_F}{D}, \tag{5}$$

where $\frac{1}{T_2^0}$ is the bulk damping constant, A includes details of the scattering process, v_F is the Fermi velocity, and D is the diameter of the NP. Since the damping rate is inversely proportional to the diameter of the NP, the effect of surface scattering decreases as the size of the NP increases. It is generally believed that the effect is dominant primarily for noble metal (Ag, Au)

NPs with diameter less than ~40 nm.[36] As the NP size increases, the percentage contribution of size to dephasing rate decreases very rapidly (the dephasing rate drops by a factor of 10 on increasing the NP size from 10 nm to 100 nm). Since our work involved Ag nanoparticles with size range between ~20 to 200 nm in diameter, we could safely assume that surface scattering was negligible in the overall contribution to the size dependent bandwidth or quality factor changes observed experimentally [for example, in Fig. 1(c)]. A second approximation that could be used was related to the quantitative value of the bulk elastic dephasing energy for Ag metal, which is ~0.02 eV.[34] When this value was compared to the measured values of the bandwidth [for example, in Fig. 1(c)], it was clear that the bulk elastic dephasing is a negligible component of the total dephasing rate and so could be neglected in all our subsequent analysis. Based on this first simplification, the bandwidth could now be written as

$$\Gamma_2 = \frac{1}{2}\Gamma_{1,R} + \frac{1}{2}\Gamma_{1,NR}. \tag{6}$$

2. *Dipolar approximation*: It has been shown by Wokaun and co-workers[37] that in the dipolar approximation, the radiative loss of nanoparticles at a fixed resonance energy is directly related to the volume of the particle V as $\Gamma_{1R}(E_{res,}V) = KV$, where K is a volume independent proportionality term. K is a material specific parameter of the individual metal and is independent of shape, size, and the ambient dielectric. In the dipolar approximation, assumed to be valid in the size range where $\frac{V}{\lambda^3} \ll 1$, where λ is the incident wavelength, the polarizability of the nanostructure is dominated by the dipolar components, as opposed to higher order multipoles. The experimental conditions of our work clearly permitted us to apply this approximation as all possible combinations of particle volume and resonance energy range investigated here had $\frac{V}{\lambda^3} \leq 10^{-2}$. This approximation was also used by Sonnichsen *et al.* to successfully interpret the radiative and non-radiative loss as a function of shape in mono-metallic Au nanostructures.[10] Likewise, in our work, for a fixed resonance energy, the two-level model could be used to establish an independent value of the non-radiative component for any given experimentally measured total bandwidth Γ_2^{Expt} as

$$\frac{1}{2}\Gamma_{1,NR}^{Eres} = \Gamma_2^{Expt}(E_{res,}V) + \frac{1}{2}\Gamma_{1,R}^{E_{res}}(V), \tag{7}$$

provided that the radiative component $\Gamma_{1,R}^{E_{res}}$ could be established for all desired combinations of resonance energy and volume.

A. Estimation of radiative dephasing rate

Based on Eq. (7), the experimentally measured bandwidth can be utilized to extract the radiative and non-radiative components, provided independent measurements of the total bandwidth can be made with a fixed volume and varying plasmon energy or vice-versa. Here we have performed this decoupling of the two contributions by varying the energy of the plasmon resonance through change in the volume of the Ag nanoparticle. This was done by preparing triangular shaped truncated pyramid nanoparticles of Ag using the nanosphere lithography (NSL) process, which has been described earlier.[38] In Fig. 5(a) a representative SEM image for the nanotriangles synthesized using a closed packed array of 200 nm diameter polystyrene (PS) beads as a shadow mask is shown. Fig. 5(b) shows the absorption spectrum for different volumes of the Ag nanotriangles, achieved by changing the base of the triangle and keeping the height of the triangle fixed at 25 nm. This was achieved by forming the triangles with NSL using PS beads of size 100, 200, and 500 nm diameter. The plasmon resonance energy decreased on increasing the volume of the triangle. This behavior is consistent with the observations that upon increasing the aspect ratio of a nanostructure, the plasmon resonance energy red shifts.[39] The height and the base of the nanotriangles were varied to generate the plasmon resonance energy of the triangles in the 2–3 eV range, shown in Fig. 5(c) as red solid triangles.

Next, we compared the bandwidth of the Ag triangles with the Ag nanoparticles as a function of the resonance energy for values measured in air ambient, as shown in Fig. 5(c). It was observed that as the plasmon resonance energy increased, the bandwidth for the hemisphere decreased while for the

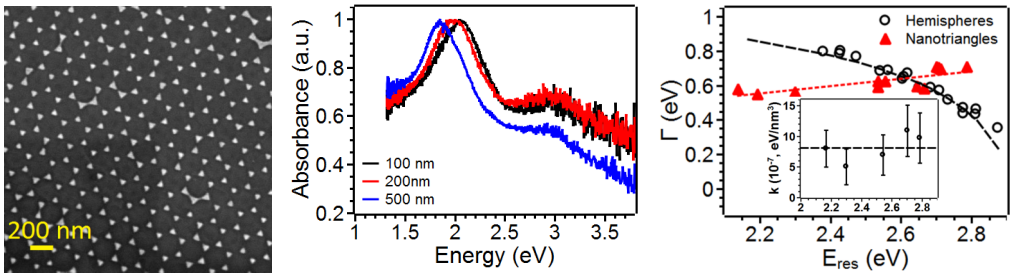

FIG. 5. (a) SEM image of the Ag nanotriangle array synthesized by NSL using a template of 200 nm PS beads with the height of the triangles equal to 25 nm. (b) Normalized absorption spectrums of Ag nanotriangles of height 25 nm formed by PS bead templates of 100, 200, and 500 nm. As the size of the PS bead is increased, the Ag plasmon shifts toward lower energy (red shifts). (c) Comparison of the BW of hemispherical Ag NPs with Ag nanotriangles plotted against the plasmon energy. The inset plots the K values calculated at the different plasmon resonance energies. The dotted line represents the average K value for the data set plotted and the dashed line represents the best fit. The x-axis of the inset is in eV.

nanotriangles, it increased. More importantly, from the data in Fig. 5(c) it was possible to extract the direct contribution of the radiative energy to the bandwidth as follows. As mentioned previously, in the dipolar approximation, the difference in bandwidth for a given energy can only come from a difference in volume and this can be used to explicitly calculate the radiative component via $\Delta\Gamma_{1,R}(E_{Res}) = K\Delta V$. From Fig. 5(c), we estimated the bandwidth difference arising from the volume difference between the hemisphere and triangle for various values of the resonance energy. The magnitude of the calculated K values at different resonance energies is shown by the open symbols in the inset of Fig. 5(c). Within the experimental uncertainty of the volume estimates, from which the error bars shown in Fig. 5(c)(inset) were generated, no significant variation in K with E_{res} was observable over this energy range and an average K value of $8.1 \pm 2.3 \times 10^{-7}$ eV/nm^3 was obtained. From this average K, it is now possible to explicitly estimate the radiative and non-radiative contributions for the various Ag nanoparticles, and this is shown in Fig. 6(a) as a function of the resonance energy and in Fig. 6(b) as a function of the particle volume.

B. Ag vs CoAg: Radiative and non-radiative contributions

Having established the values of the radiative and non-radiative contributions to the plasmon bandwidth in pure Ag, we can now interpret the behavior of CoAg. As has been detailed previously, the CoAg bimetal consists of distinctly segregated regions of Ag and Co, due to their immiscibility.[22–25] In other words, the Ag region is identical to pure Ag in its composition. On this basis, one would expect that, for the Ag region, the intrinsic loss effects such as bulk elastic dephasing rate and the non-radiative contribution to the dephasing should be identical to that of pure Ag. Overall, since the total bandwidth is an additive sum of the various contributions, we considered that the overall response of a Co+Ag nanoparticle should be the sum of various contributions as

$$\Gamma_2^{\mathrm{Ag+Co}} = 2^{-1}(\Gamma_{1,R}^{\mathrm{Ag}} + \Gamma_{1,R}^{\mathrm{Co}}) + 2^{-1}(\Gamma_{1,NR}^{\mathrm{Ag}} + \Gamma_{1,NR}^{\mathrm{Co}}) + \Gamma_2^{\mathrm{Ag*}} + \Gamma_2^{\mathrm{Co*}}. \quad (8)$$

We mentioned previously that the non-radiative contribution from Co must be significantly larger than that of Ag, and hence irrespective of the other contributions from Co, the overall bandwidth for the CoAg nanoparticles should be larger than the pure Ag case. Therefore, the quality factor of the CoAg must be lower for given energy and volume in comparison to that of the pure Ag. However, as we saw from Fig. 3, the quality factor for the CoAg system can be comparable to or even be larger than pure Ag for energies from 2.3 to 2.7 eV [Fig. 3(c)] or volumes from 1 to 2×10^5 nm^3 [Fig. 3(b)]. Clearly, this is not consistent with the predictions from Eq. (8). We could also neglect the role of near-field coupling (typically observed when the spacing between particles is within a few nanometers or <<D) on influencing the bandwidth behaviors,[12] since in our case, the average spacing between the NPs in the arrays was $\geq D$.

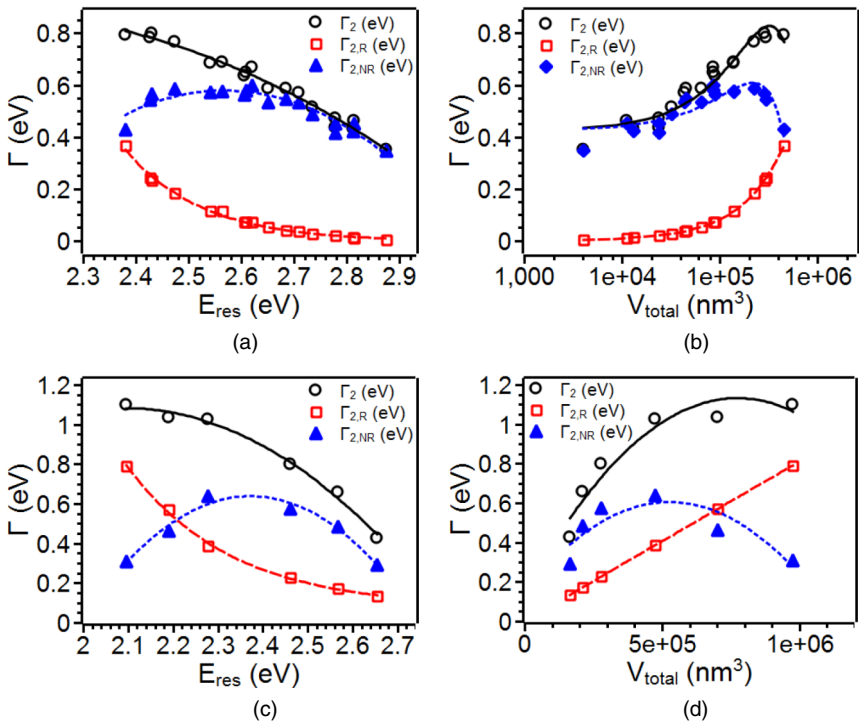

FIG. 6. Radiative and non-radiative contributions to the total bandwidth of Ag NPs. (a) Energy dependence of the bandwidth contributions. (b) Volume dependence of the bandwidth contributions (note log scale on x-axis). Radiative and non-radiative contributions to the total bandwidth of bimetallic NPs. (c) Energy dependence of bandwidth contributions for CoAg. (d) Volume dependence of the bandwidth contributions for CoAg (note log scale on x-axis).

We propose that one way to understand the unusual behavior of the CoAg system is that the Co nanoparticle in contact with Ag modifies the radiative bandwidth of the Ag plasmonic nanoparticle. While such effects are known to occur in coupled pairs of molecules and nanoparticles with well defined absorption levels,[40,41] there is no prior evidence that it can occur in two contacted metallic nanoparticles with significantly different plasmonic character i.e., one is strongly plasmonic (Ag) while the other is not (Co). However, recently, we reported electron energy loss investigations in a transmission electron microscope that showed evidence for unusually strong coupling between the two metals that resulted in a strong plasmonic signature within the Co side of the bimetal nanostructure.[24] Here, to estimate the contribution of the radiative component, we assumed that the CoAg behaves like a Ag nanoparticle and calculated the modified radiative BW by assuming the entire CoAg NP to be a pure Ag NP. After calculating the radiative BW, the non-radiative BW component was calculated as $\Gamma_{1,NR}^{CoAg} = \Gamma^{CoAg} - \Gamma_{1,R}^{Ag}$. The result of this analysis is shown in Figs. 6(c) and 6(d) for the CoAg. From this analysis the non-radiative loss was found to be larger than the radiative contribution for energies $\gtrsim$2.2 eV and volumes $\leq 5.4 \times 10^5$ nm^3.

To explain the radiative BW modification of Ag in contact with Co, we utilized the analytical model presented by Tsakmakidis *et al.*[42] This model describes the interaction of two nonbianisotropic systems placed adjacent to each other within the interaction regime consisting of poor and good conductors. The metamaterial system is depicted and explained using an equivalent R-L-C electrical circuit as described in Fig. 3 of Ref. 42. Here, Co and Ag are considered as the equivalents of poor and good conductors, respectively. To explain our results, we have followed the approach presented by Tsakmakidis *et al.*, with a slight modification. In our case, the amount of Ag is fixed, but the amount of Co is varied. To accommodate the change in the Co amount, we assumed the dependence of surface to volume ratio in the various parameters used in the model rather than in the surface area. We then calculated the active power, $P = P_1 + P_2$, which is the summation of the individual active powers of

Co and Ag. The active power was calculated as

$$P_l = Re\left\{V_l I_l^{\star}\right\}, \tag{9}$$

where, $l = 1,2$ and V is the voltage and I is the current which are defined as

$$V_l = -i\omega\mu_0 S_l H_0, \tag{10}$$

$$I_l = \frac{det\,(G_l)}{det\,(G)}, \tag{11}$$

where ω is the frequency, μ_0 is the permeability, S is the surface to volume ratio, and H_0 is the amplitude of the magnetic component of the electromagnetic wave. G_l and G are defined as

$$G_1 = \begin{bmatrix} V_1 & i/\omega C \\ V_2 & R_2 + i\omega L_2 - i/\omega C_2 - i/\omega C \end{bmatrix}, \tag{12}$$

$$G_2 = \begin{bmatrix} R_1 + i\omega L_1 - i/\omega C_1 - i/\omega C & V_1 \\ i/\omega C & V_2 \end{bmatrix}, \tag{13}$$

$$G = \begin{bmatrix} R_1 + i\omega L_1 - i/\omega C_1 - i/\omega C & i/\omega C \\ i/\omega C & R_2 + i\omega L_2 - i/\omega C_2 - i/\omega C \end{bmatrix}. \tag{14}$$

Here, R_l is the total lumped resistance, equivalent to the sum of ohmic and radiative losses. C_l and L_l are the lumped capacitance and inductance, respectively. C is the interaction capacitance between the two metamaterials.

The total active power and the individual powers were then calculated for three different S values of Co, while keeping S fixed for Ag. The parameter values utilized in calculating the active power were $H_0 = 1$ A/m, $R_1 = 0.1\ \Omega$, $R_2 = 50\ \Omega$, $C_1 = C_2 = 10$ fF , $C = 0.1$ pF, $L_1 = L_2 = 16$ nH. S value for Ag was fixed at $4 \times \pi$ mm^{-1} while $S_1 = 2 \times \pi$ mm^{-1}, $S_2 = 4 \times \pi$ mm^{-1}, and $S_3 = 6 \times \pi$ mm^{-1} were used for Co. Fig. 7 compares the active powers of poor (Co) and good (Ag) conductors and the total power of the system. The behavior depicted by Fig. 7(a) is that, as the surface to volume ratio is increased in going from S_1 to S_3, the Co power crosses to the positive side in the 13–15 GHz range [Fig. 7(a)]. On the other hand, as the surface to volume ratio increases, the Ag power in the interacting system crosses from positive to negative [Fig. 7(b)], a trend observed opposite to that for Co in the 13–15 GHz range. For small S value, i.e., S_1, the Ag power remains positive over the frequency regime studied. This can also be observed in Fig. 7(c), in which the total active power for S_1 remains non-zero, while for the other S values, i.e., S_2 and S_3, the power goes to zero in the 13–15 GHz frequencies when $P_1 = 0$. In order for the total power to be zero at the frequency at which $P_1 = 0$, P_2 should also be zero. This suggests that the active power of Ag goes to $P_2 \approx 0$, which is only possible due to the coupling happening between Ag and Co. As the volume of Co is increased, then its surface to volume

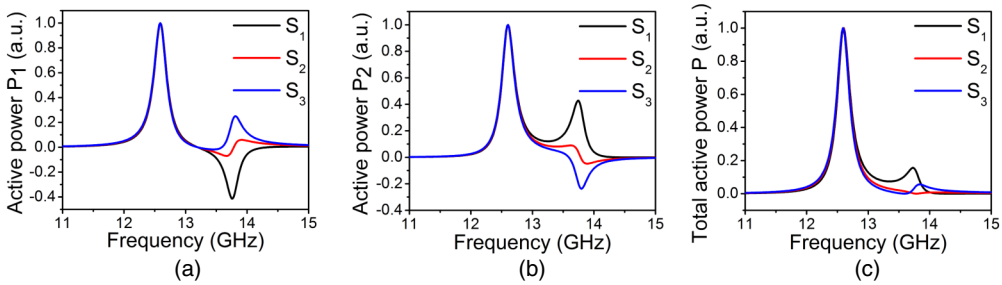

FIG. 7. Comparison of the active power in two interacting nonbianisotropic systems. (a) Active power for poor conductor (equivalent to Co), (b) good conductor (equivalent to Ag), and (c) the total power of the poor-good conductor system for three different surface to volume ratio's for poor conductor. The parameters used to calculate the active power are similar to the ones used in Ref. 42. The three different S values used to calculate the active power are $S_1 = 2 \times \pi$, $S_2 = 4 \times \pi$ and $S_3 = 6 \times \pi$ mm^{-1}.

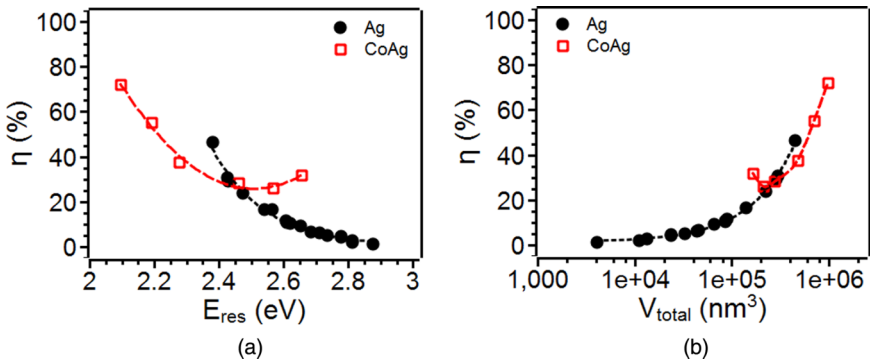

FIG. 8. Quantum Efficiency of Ag and bimetal CoAg. (a) Energy dependence of η. (b) Variation of η with total volume of nanoparticle.

ratio decreases, which results in weaker coupling as depicted in Fig. 7(c), resulting in the total active power remaining positive. This model for resonators in close vicinity suggests that when the radiation emitted from Co is suppressed ($P_1 = 0$), then it suppresses the radiation emitted by the neighbour Ag. This result can be further extended to explain the crossover in the quality factor trends shown in Fig. 3. As the Co amount is increased, the surface to volume ratio decreases resulting in a weaker coupling between Co and Ag. This leads to weakening of the suppression of radiative losses. Thus, the modification of the radiative losses effects the quantum efficiency of the bimetallic NP system, as shown in Subsection III C.

C. Quantum efficiency of plasmonic scattering from Ag and CoAg

Since the individual contributions from radiative and non-radiative decays were estimated for the pure Ag and bimetallic CoAg systems, we were able to calculate the quantum efficiency for radiative energy transfer from the plasmonic system to its surrounding as $\eta = \frac{\Gamma_{1R}}{\Gamma_{1R}+\Gamma_{1NR}}$. The quantum efficiency comparison of Ag to bimetal CoAg are shown in Fig. 8. In Fig. 8(a) the variation with resonance energy showed that η for the bimetal was comparable to Ag and could also be larger than that of Ag for energies $\gtrsim$2.5 eV. The volume dependent behaviors shown in Fig. 8(b) suggest that the bimetal systems can emulate the scattering efficiency of pure Ag nanoparticles. Several plasmonic applications require either optimizing the quality factor or the quantum efficiency independently, such as for LSPR sensing versus solar energy harvesting. Our results suggest that the Q and η can be independently controlled by varying the size and composition of the nanoparticles. Furthermore, by synthesizing bimetallic nanoparticles, the quantum efficiency (or Q factor) can be enhanced over that of pure Ag at different energy positions thus broadening the energy regime for excellent plasmonic response.

IV. CONCLUSION

In this work, we have investigated the size and energy dependence of the plasmonic quality factor in hemispherical Ag and CoAg bimetallic NPs. Optical spectroscopy studies showed that the bandwidth of the plasmon resonance from CoAg could be comparable to and even better that of pure Ag. To understand the origin of this behavior, the contribution from radiative and non-radiative effects was independently established by comparing the plasmonic behaviors of Ag hemispherical nanoparticles to Ag triangular particles. A phenomenological model comparing CoAg bimetals to Ag within the quasi-static and effective medium models reveled that the CoAg bimetal system can significantly influence the radiative energy transfer from the Ag component of the bimetal. As a consequence, the bimetallic systems could have comparable or better quality factor and or quantum efficiency to that of pure Ag in certain regimes of resonance energy and particle volume. These results demonstrate that

the bimetal nanostructures could be used to engineer the plasmonic bandwidths and thus be a viable approach to tune the quality factor and quantum efficiency of localized surface plasmon processes.

V. EXPERIMENTAL SECTION

The nanoparticles were synthesized using two different synthesis techniques. The hemispherical shaped nanoparticles were synthesized by pulsed laser dewetting. The quartz substrates were cleaned by sonicating in acetone, methanol, and deionized water for 30 min each. The substrates were then dried and were used for subsequent studies later on. Metal films of Ag and Co were deposited using electron beam evaporator in a UHV chamber with a base pressure of 2×10^{-8} Torr. Ag films of thickness 1-10 nm were deposited for the dewetting studies and for the bimetal nanoparticles synthesis Ag film was fixed at 5 nm and the Co film thickness was varied between 1-5 nm. The bilayer films were deposited in a sequential order with Co on top of Ag film. The deposited metal films were than rastered using a 9 ns pulsed Nd:YAG laser operating at 50 Hz, at 266 nm. Areas of approximately 1-5 mm^2 area were rastered (at ~2 mm/min) at energy density of 80-90 and 100-110 mJ/cm^2 for Ag and CoAg films, respectively. The diameter of the gaussian profile laser spot was 1 mm. The triangular shaped nanostructures were synthesized using nanosphere lithography technique (NSL). The mask formation was done either by spincoating or by formation of polystyrene (PS) mask at the air-water interface. The details for the PS mask formation by spincoating can be found in the following Ref. 38. PS beads of diameter 500 nm were used to form mask using this technique. The other technique for PS mask formation at the air-water interface was done according to the Refs. 43–45. Sodium dodecyl sulfate (SDS) was dissolved in water to make a solution of 0.3M concentration. After which equal volumes of PS beads solution (sizes 100 or 200 nm) were mixed with ethanol. The SDS solution was filled in a glass trough and the PS beads solution was poured onto a glass slide inclined at ~45° angle and partially immersed in the trough. A syringe was used to pour the PS solution on the glass slide. Using this technique, large patches of PS monolayer of size in cm range were formed at the air-water interface. The PS monolayers were transferred onto the substrate by scooping the PS monolayer and then were left for drying at an inclination angle of 2°-4° in a controlled environment. Using this technique, continuous monolayer patches of cm square area can be achieved. After the PS mask formation, Ag films in the range from 15-50 nm deposited through the PS mask and the mask was etched out to give the final nanostructures of triangular shapes.

The scanning electron microscope (SEM) imaging of the nanostructures were done using Zeiss Merlin being operated in 1-5 kV range using a SE detector. The optical measurements were obtained in transmission mode using HR2000+ES spectrometer. The transmission spectrums were then converted to absorption spectrums using Beer-Lambert's law and were then normalized. The normalized absorption spectrums were fitted with single Lorentzian curves to extract the BW for the plasmon resonance.

SUPPLEMENTARY MATERIAL

See supplementary material for the details of the Lorentz fits, optical properties of the Ag nanotriangles, contributions of electron dephasing on the bandwidth, the role of particle spacing on the bandwidth, and the error bar calculations.

ACKNOWLEDGMENTS

The authors acknowledge support by the Army Research Office through Grant No. W911NF-13-1-0428. A portion of this research was conducted under Grant No. CNMS2013-284 at the Center for Nanophase Materials Science, which is sponsored at ORNL by the Scientific User Facilities Division, Office of Basic Energy Sciences, U.S. Department of Energy.

[1] S. A. Maier, *Plasmonics: Fundamentals and Applications* (Springer, New York, 2007).
[2] H. A. Atwater and A. Polman, "Plasmonics for improved photovoltaic devices," Nat. Mater. **9**, 205–213 (2010).
[3] D. O'Connor and A. V. Zayats, "Data storage: The third plasmonic revolution," Nat. Nanotechnol. **5**, 482–483 (2010).

[4] P. K. Jain, X. Huang, I. H. El-Sayed, and M. A. El-Sayed, "Noble metals on the nanoscale: Optical and photothermal properties and some applications in imaging, sensing, biology, and medicine," Acc. Chem. Res. **41**, 1578–1586 (2008).
[5] K. Appavoo, B. Wang, N. F. Brady, M. Seo, J. Nag, R. P. Prasankumar, D. J. Hilton, S. T. Pantelides, and R. F. Haglund, Jr., "Ultrafast phase transition via catastrophic phonon collapse driven by plasmonic hot-electron injection," Nano Lett. **14**, 1127–1133 (2014).
[6] S. Grillanda and F. Morichetti, "Light-induced metal-like surface of silicon photonic waveguides," Nat. Commun. **6**, 8182 (2015).
[7] P. K. Jain, K. S. Lee, I. H. El-Sayed, and M. A. El-Sayed, "Calculated absorption and scattering properties of gold nanoparticles of different size, shape, and composition: Applications in biological imaging and biomedicine," J. Phys. Chem. B **110**, 7238–7248 (2006).
[8] S. Neatu, J. A. Macia-Agullo, P. Concepcion, and H. Garcia, "Gold-copper nanoalloys supported on TiO_2 as photocatalysts for CO_2 reduction by water," J. Am. Chem. Soc. **136**, 15969–15976 (2014).
[9] N. Passarelli, L. A. Perez, and E. A. Coronado, "Plasmonic interactions: From molecular plasmonics and fano resonances to ferroplasmons," ACS Nano **8**, 9723–9728 (2014).
[10] C. Sonnichsen, T. Franzl, T. Wilk, G. von Plessen, J. Feldmann, O. Wilson, and P. Mulvaney, "Drastic reduction of plasmon damping in gold nanorods," Phys. Rev. Lett. **88**, 077402 (2002).
[11] F. Wang and Y. R. Shen, "General properties of local plasmons in metal nanostructures," Phys. Rev. Lett. **97**, 206806 (2006).
[12] C. Dahmen, B. Schmidt, and G. von Plessen, "Radiation damping in metal nanoparticle pairs," Nano Lett. **7**, 318–322 (2007).
[13] O. Pena-Rodriguez and U. Pal, "Au@Ag core-shell nanoparticles: Efficient all-plasmonic Fano-resonance generators," Nanoscale **3**, 3609 (2011).
[14] L. Wang, Z. Clavero, C. Huba, K. J. Carroll, E. E. Carpenter, D. Gu, and R. A. Lukaszew, "Plasmonics and enhanced magneto-optics in core-shell Co-Ag nanoparticles," Nano Lett. **11**, 1237–1240 (2011).
[15] D. Meneses-Rodriguez, E. Ferreiro-Vila, P. Prieto, J. Anguita, M. U. Gonzalez, J. M. Garcia-Martin, A. Cebollada, A. Garcia-Martin, and G. Armelles, "Probing the electromagnetic field distribution within a metallic nanodisk," Small **7**, 3317–3323 (2011).
[16] G. A. Sotiriou, A. M. Hirt, P. Y. Lozach, A. Teleki, F. Krumeich, and S. E. Pratsinis, "Hybrid, silica-coated, janus-like plasmonic-magnetic nanoparticles," Chem. Mater. **23**, 1985–1992 (2011).
[17] Y. Sato, S. Naya, and H. Tada, "A new bimetallic plasmonic photocatalyst consisting of gold(core)-copper(shell) nanoparticle and titanium(IV) oxide support," APL Mater. **3**, 104502 (2015).
[18] A. J. McGrath, Y. H. Chien, S. Cheong, D. A. J. Herman, J. Watt, A. M. Henning, L. Gloag, C. S. Yeh, and R. D. Tilley, "Gold over branched palladium nanostructures for photothermal cancer therapy," ACS Nano **9**, 12283–12291 (2015).
[19] B. N. Khlebtsov, Z. Liu, J. Ye, and N. G. Khlebtsov, "Au@ag core/shell cuboids and dumbbells: Optical properties and sers response," J. Quant. Spectrosc. Radiat. Transfer **167**, 64–75 (2015).
[20] G. Armelles, A. Cebollada, A. Garcia-Martin, J. M. Garcia-Martin, M. U. Gonzalez, J. B. Gonzalez-Diaz, E. Ferreiro-Vila, and J. F. Torrado, "Magnetoplasmonic nanostructures: Systems supporting both plasmonic and magnetic properties," J. Opt. A: Pure Appl. Opt. **11**, 114023 (2009).
[21] H. Krishna, J. Strader, A. K. Gangopadhyay, and R. Kalyanaraman, "Nanosecond laser-induced synthesis of nanoparticles with tailorable magnetic anisotropy," J. Magn. Magn. Mater. **323**, 356–362 (2011).
[22] R. Sachan, S. Yadavali, N. Shirato, H. Krishna, V. Ramos, G. Duscher, S. J. Pennycook, A. K. Gangopadhyay, H. Garcia, and R. Kalyanaraman, "Self-organized bimetallic Ag-Co nanoparticles with tunable localized surface plasmons showing high environmental stability and sensitivity," Nanotechnology **23**, 275604 (2012).
[23] R. Sachan, V. Ramos, A. Malasi, B. Bartley, G. Duscher, and R. Kalyanaraman, "Oxidation resistant Ag nanoparticles for ultrastable plasmonic applications," Adv. Mater. **25**, 2045–2050 (2013).
[24] R. Sachan, A. Malasi, J. Ge, S. Yadavali, H. Krishna, A. Gangopadhyay, H. Garcia, G. Duscher, and R. Kalyanaraman, "Ferroplasmons: Intense localized surface plasmons in metal-ferromagnetic nanoparticles," ACS Nano **8**, 9790–9798 (2014).
[25] R. Sachan, A. Malasi, S. Yadavali, B. Griffey, J. Dunlap, G. Duscher, and R. Kalyanaraman, "Laser induced self-assembled nanostructures on electron transparent substrates," Part. Part. Syst. Charact. **32**, 476–482 (2015).
[26] A. Malasi, R. Sachan, V. Ramos, H. Garcia, G. Duscher, and R. Kalaynaraman, "Localized surface plasmon sensing based investigation of nanoscale metal oxidation kinetics," Nanotechnology **26**, 205701 (2015).
[27] H. Krishna, N. Shirato, S. Yadavali, R. Sachan, J. Strader, and R. Kalyanaraman, "Self-organization of nanoscale multilayer liquid metal films: Experiment and theory," ACS Nano **5**, 470–476 (2011).
[28] H. Garcia, R. Sachan, and R. Kalyanaraman, "Optical plasmon properties of Co-Ag nanocomposites within the mean-field approximation," Plasmonics **7**, 137–141 (2012).
[29] M. Blaber, M. Arnold, and M. Ford, "A review of the optical properties of alloys and intermetallics for plasmonics," J. Phys.: Condens. Matter **22**, 143201 (2010).
[30] P. Offermans, S. R. K. Schaafsma, M. C. Rodriguez, Y. Zhang, M. Crego-Calama, S. H. Brongersma, and J. G. Rivas, "Universal scaling of the figure of merit of plasmonic sensors," ACS Nano **5**, 5151–5157 (2011).
[31] H. Garcia, J. Trice, R. Kalyanaraman, and R. Sureshkumar, "Self-consistent determination of plasmonic resonances in ternary nanocomposites," Phys. Rev. B **75**, 045439 (2007).
[32] A. Malasi, R. Kalyanaraman, and H. Garcia, "From Mie to Fresnel through effective medium approximation with multipole contributions," J. Opt. **16**(6), 065001 (2014).
[33] E. J. Heilweil and R. M. Hochstrasser, "Nonlinear spectroscopy and picosecond transient grating study of colloidal gold," J. Chem. Phys. **82**, 4762–4770 (1985).
[34] P. R. West, S. Ishii, G. V. Naik, N. K. Emani, V. M. Shalaev, and A. Boltasseva, "Searching for better plasmonic materials," Laser Photonics Rev. **4**, 795–808 (2010).
[35] S. Link and M. El-Sayed, "Spectral properties and relaxation dynamics of surface plasmon electronic oscillations in gold and silver nanodots and nanorods," J. Phys. Chem. B **103**, 8410–8426 (1999).
[36] S. Link and M. A. El-Sayed, "Shape and size dependence of radiative, non-radiative and photothermal properties of gold nanocrystals," Int. Rev. Phys. Chem. **19**, 409–453 (2000).

[37] A. Wokaun, J. P. Gordon, and P. F. Liao, "Radiation damping in surfcae-enhanced raman-scattering," Phys. Rev. Lett. **48**, 957–960 (1982).
[38] A. Malasi, J. Ge, C. Carr, H. Garcia, G. Duscher, and R. Kalyanaraman, "Two-dimensionally ordered plasmonic and magnetic nanostructures on transferable electron transparent substrates," Part. Part. Syst. Charact. **32**, 970–978 (2015).
[39] K. L. Shuford, M. A. Ratner, and G. C. Schatz, "Multipolar excitation in triangular nanoprisms," J. Chem. Phys. **123**, 114713 (2005).
[40] J. R. Lakowicz, "Radiative decay engineering: Biophysical and biomedical applications," Anal. Biochem. **298**, 1–24 (2001).
[41] Q. Hao, D. Du, C. Wang, W. Li, H. Huang, J. Li, T. Qiu, and P. K. Chu, "Plasmon-induced broadband fluorescence enhancement on Al-Ag bimetallic substrates," Sci. Rep. **4**, 6014 (2014).
[42] K. L. Tsakmakidis, M. S. Wartak, J. J. H. Cook, J. M. Hamm, and O. Hess, "Negative-permeability electromagnetically induced transparent and magnetically active metamaterials," Phys. Rev. B **81**, 195128 (2010).
[43] X. Meng and D. Qiu, "Gas-flow-induced reorientation to centimeter-sized two-dimensional colloidal single crystal of polystyrene particle," Langmuir **30**, 3019–3023 (2014).
[44] N. Vogel, S. Goerres, K. Landfester, and C. K. Weiss, "A convenient method to produce close-and non-close-packed monolayers using direct assembly at the air-water interface and subsequent plasma-induced size reduction," Macromol. Chem. Phys. **212**, 1719–1734 (2011).
[45] P. Moitra, B. A. Slovick, W. Li, I. I. Kravchencko, D. P. Briggs, S. Krishnamurthy, and J. Valentine, "Large-scale all-dielectric metamaterial perfect reflectors," ACS Photonics **2**, 692–698 (2015).